



This is the accepted manuscript made available via CHORUS. The article has been published as:

Skymion-Based Programmable Logic Device with Complete Boolean Logic Functions

Z.R. Yan, Y.Z. Liu, Y. Guang, K. Yue, J.F. Feng, R.K. Lake, G.Q. Yu, and X.F. Han

Phys. Rev. Applied **15**, 064004 — Published 2 June 2021

DOI: [10.1103/PhysRevApplied.15.064004](https://doi.org/10.1103/PhysRevApplied.15.064004)

Skyrmion-based Programmable Logic Device with Complete Boolean Logic Functions

Z. R. Yan^{1,2}, Y. Z. Liu^{1,2}, Y. Guang^{1,2}, K. Yue³, J. F. Feng^{1,2}, R. K. Lake⁴, G. Q. Yu^{1,2,5}
, and X. F. Han^{1,2,5}

¹Beijing National Laboratory for Condensed Matter Physics, Institute of Physics,

Chinese Academy of Sciences, Beijing 100190, China

²Center of Materials Science and Optoelectronics Engineering, University of

Chinese Academy of Sciences, Beijing 100049, China

³Ming Hsieh Department of Electrical and Computer Engineering, University of

Southern California, Los Angeles, CA 90089, USA

⁴Department of Electrical and Computer Engineering, University of California,

Riverside, California 92521, USA

⁵Songshan Lake Materials Laboratory, Dongguan, Guangdong 523808, China

Email address: guoqiangyu@iphy.ac.cn, xfhan@iphy.ac.cn

Keywords: Skyrmion, Exchange bias, Logic

A skyrmionic programmable logic device (SkrPLD) with complete Boolean logic functions is proposed and analyzed by micromagnetic simulations. The SkrPLD is based on an antiferromagnet/ferromagnet bilayer structure, in which the antiferromagnetic layer supports the interfacial Dzyaloshinskii–Moriya interaction and the out-of-plane exchange bias field for stabilizing a zero-field skyrmion. By varying the local exchange bias field, artificial pinning sites are introduced for trapping the skyrmions. Depending on the input currents and the initial position of skyrmions at different pinning sites, different logic functions can be realized. Micromagnetic simulations show that the proposed SkrPLD has robust performance even under thermal fluctuations and inhomogeneity effects. Our work can provide insights for the design of programmable spin logic devices.

I. INTRODUCTION

Magnetic order that can be harnessed via magnetic field or electrical current has been widely explored for memory, logic, and sensor applications [1-5]. The demand for scaling down the size of magnetic device grows as the developments of information processing and storage technologies. To this end, nano-sized magnetic textures have been extensively studied with promising prospects on dense magnetic devices. A magnetic skyrmion is a newly discovered topological magnetic texture, which has received much attention due to its prominent properties, such as nanoscale size, non-trivial topology, and low driving current density [5-10]. These properties have led to the proposals for a range of prototypes of skyrmionic devices, such as skyrmion racetrack memory [5,8,10-12] and skyrmion logic [13-17].

Boolean logic devices comprise the basic elements in modern electronic circuits. Conventional logic devices can be classified into two broad categories: fixed logic device (FLD) and programmable logic device (PLD) [18]. In recent years, many FLDs that are based on magnetic devices have been proposed. For example, a single magnetic domain, domain wall, or skyrmion can be employed as information bits to achieve different logic functionalities in FLD [13-17,19-26]. However, the logic functionality of FLD is fixed once being manufactured, which limits the flexibility in applications. In contrast, a PLD can be reconfigured and hence possesses multiple functionalities. Nonetheless, there are only a few research works reporting the realization of a skyrmion-based PLD [16]. Similar to the racetrack device, in a skyrmionic programmable logic device (SkrPLD), the input and output binary data bits “1” and “0”

are encoded by the state with and without a skyrmion, respectively. Based on the voltage-controlled magnetic anisotropy effect, some SkrPLDs have been proposed [16,17]. However, racetrack-based devices may suffer from the skyrmion Hall effect (SkrHE), thermal fluctuations, and edge roughness, especially in constricted devices [7,12,27-31].

Here, we report a SkrPLD with complete Boolean logic functions (16 functions including AND, NAND, XOR, etc.) based on artificially induced skyrmion pinning sites and current-driven skyrmion motion. Depending on the initial skyrmion position and applied currents, full logic functionalities can be achieved. The proposed scheme does not suffer from the SkrHE and skyrmion-edge repulsion since the working principle does not involve long-range skyrmion diffusion and skyrmion-edge interaction. Furthermore, simulations with thermal fluctuations and inhomogeneity effects also demonstrate the robustness of the proposed SkrPLD device.

II. MODEL AND METHOD

The proposed logic device is shown in Fig. 1(a). The antiferromagnet (AFM)-based heterostructure is patterned into a crossbar with the center region of $400 \times 450 \text{ nm}^2$. The antiferromagnetic layer provides the interfacial Dzyaloshinskii–Moriya interaction and an exchange bias field to the ferromagnetic (FM) layer for which endows zero-field stability to the skyrmion. Electrical currents are designed as input signals with identical amplitude, I_1 and I_2 , which are orthogonal to each other. Due to the spin Hall effect in the AFM layer[32-37], the applied current generates spin-orbit torque and drives the

skyrmion motion in the FM layer [8,38,39]. To achieve different logic functions, the skyrmions must be initialized in the ferromagnetic layer by injecting a spin-polarized current through four different magnetic tunnel junctions (MTJs) marked as A, B, C, and D. The MTJ D is also used for reading the skyrmion as the output signal via the tunneling magnetoresistance (TMR) [9,10]. As shown in Figs. 1b and c, the FM layer that hosts the skyrmions serves as the free layer of the MTJ, and the TMR is determined by the relative magnetization state between the FM layer and the fixed layer of the MTJ. The presence (absence) of a skyrmion can be defined as the high (low) resistance state. The local exchange bias field can be manipulated by scanning tip-based field cooling[40], X-ray exposure[41], or electron beam to achieve effective pinning for the skyrmion [42]. Figure 1(d) shows the layout of pinning sites and MTJs. These pinning sites are designed for positioning the skyrmions. The input currents determine the direction of skyrmion motion associated with the SkrHE [7,30,31]. In the proposed device, we set the skyrmion Hall angle (θ_{SkrHE}) $\sim 45^\circ$ for clarity and this parameter can be optimized for different materials. Figures 1(e)–(h) show the direction of skyrmion motion under different input current schemes. The influence of different θ_{SkrHE} will be discussed later.

To simulate the skyrmion motion and design the skyrmionic programmable logic device, the micromagnetic simulation package Mumax3 is employed [43]. In the simulation, the magnetic system is discretized into a mesh of dimensions $1 \text{ nm} \times 1 \text{ nm} \times 1 \text{ nm}$. The material-related parameters are: the saturation magnetization (M_S) $1.0 \times 10^6 \text{ A/m}$, the exchange stiffness constant (A) $1.5 \times 10^{-11} \text{ J/m}$, the Dzyaloshinskii-Moriya

constant (D) 2 mJ/m^2 , the perpendicular magnetic anisotropy (PMA) constant (K_u) $0.9 \times 10^6 \text{ J/m}^3$, the spin Hall angle (θ_{SHE}) 0.4 , and the damping coefficient (α) 0.3 , respectively. The dipole-dipole interaction is also considered. The working principle of the proposed device is irrespective of the edge, and hence we do not consider the edge effect. The periodic boundary condition is adopted to improve the simulation efficiency (for more details of the simulations with larger area and open boundary condition, see Appendix B). The pinning site induced by the local exchange bias field (LEBF) serves as an effective potential well for the skyrmion. Such a pinning effect has been systematically investigated in our previous work[12]. It is shown that the pinning strength can be engineered by the size of the potential well (D_E) and the intensity of the exchange-bias field (H_E). For large D_E and H_E , the pinning effect is strong and the skyrmion is easily trapped by the pinning site. In our model, D_E is 60 nm and the nearest distance between different pinning sites is $240/\sqrt{2} \text{ nm}$. The effective local exchange bias field H_E in the circle is 0.02 T (field direction along y axis because the Néel orders are reconfigured by local thermal excitations induced by X-ray exposure [41] or electron beam [42] and finally points to the $+y$ direction) while the H_E outside the circular pinning region is 0.02 T (field direction along z axis because the Néel orders in AFM layer is initially uniformly points to the $+z$ direction). We consider a layered AFM and assume the LEBF is not affected by the magnetization dynamics in FM layer [41,42]. Thermal fluctuations ($\sim 300 \text{ K}$) are included. The effect of inhomogeneity is introduced by a 5% variation of saturation magnetization, exchange stiffness constant, DMI constant, and anisotropy in different grains (grain size $\sim 10 \text{ nm}$).

III. SKYRMION-BASED PROGRAMMABLE LOGIC GATES

We first explain the working principle of the logic operation for a XOR gate as an example. As shown in Fig. 2(a1), the clean operation is first executed by applying a large current pulse ($\sim 10^{12}$ A/m²) to annihilate skyrmions on all the MTJ sites. This operation can wipe out previously configured functions. To initialize the XOR function, two skyrmions are created at positions B and C by local injection of a spin-polarized current [Fig. 2(a2)]. Then, electric current pulses with duration $t_p = 1.5$ ns and density $J_p = 2 \times 10^{11}$ A/m² are injected as inputs. For the case with input signal $I_1 = 0$ and $I_2 = 0$ [Fig. 2 (a3)], no electric current is injected and the skyrmions stay in their original position. Therefore, a low resistance state in MTJ D is read out, showing the output signal of ‘R = 0’ as shown in Fig. 2(a4). Figures 2(b1), (c1), and (d1) show the results for different combinations of the input signal. If the input signal is $I_1 = 0$ ($I_1 = 1$) and $I_2 = 1$ ($I_2 = 0$) as shown in Fig. 1(b3) [Fig.1 (c3)], the applied in-plane current flows along y (x) axis and the skyrmions both move along the vector $(-1, 1)$ $[(1, 1)]$. After the injection of the input current pulse, the skyrmion in B (C) site moves to the D site. Finally, the high resistance state in MTJ D is read out, showing an output signal of ‘R = 1’ (Figs. 2(b4) and (c4)). As for the case with $I_1 = 1$ and $I_2 = 1$ which is similar to the case of $I_1 = 0$ and $I_2 = 0$, no skyrmion moves into D site, as a result ‘R = 0’ [Fig. 1 (d4)].

In Fig. 3, we show the simulation results for several other logic gates. Different initial skyrmion configuration corresponds to different logic operation. For example, initializing skyrmion in B and C sites leads to the function of the XOR logic gate as discussed above. The initialization of skyrmions at sites A, D, AD, BC, ABC, and BCD

leads to AND, NOR, NXOR, XOR, OR, and NAND logic gate, respectively. It should be noted that the device also has stable performance under thermal fluctuations (300K) and inhomogeneity effects. The proposed device can realize sixteen logic functions (see table I), including material implication comparator [B for inverse implication (NIMP), C for reverse inverse implication (RNIMP), ACD for inverse implication (IMP) and ABD for reverse implication (RIMP)], inoperation (AB for I_1 and AC for I_2), NOT gate (BD for NOT I_2 and CD for NOT I_1), False (no skyrmion set), and True (ABCD).

IV. DISCUSSIONS

A. Influences of θ_{SkrHE} and θ_{SHE}

The examples discussed above show that the skyrmion shift operation determines the output signal, indicating that the logic operation relies on stable skyrmion positioning and precise skyrmion shift operation. Thus, θ_{SkrHE} is an important parameter in this device. For specific values of θ_{SkrHE} , the design of the layout of pinning sites and MTJs should be further optimized, as shown in appendix Figs. 5(d) and (h) and Fig. 6. On the other hand, θ_{SHE} also influences the amplitude and duration of input current pulse and is closely related to the operation frequency.

To further understand the role of θ_{SHE} and the magnitude of the input current pulse J_p , we employ the Thiele's approach [8,38,39]. Their relationship can be obtained by the Thiele equation

$$\vec{\mathbf{G}} \times \vec{\mathbf{v}} - \alpha \vec{\mathbf{D}} \cdot \vec{\mathbf{v}} + 4\pi B \vec{\mathbf{R}} \cdot \vec{\mathbf{J}} = 0 \quad (1)$$

Here the $\vec{\mathbf{G}} = (0, 0, g)$ is gyrocoupling vector with $g = 4\pi$, $\vec{\mathbf{v}} = (v_x, v_y)$ is the

velocity of the skyrmion, $\vec{J} = (J_p, 0)$ is the current density. $\vec{D} = \begin{bmatrix} D_0 & 0 \\ 0 & D_0 \end{bmatrix}$ is the dissipative tensor and $\vec{R} = \begin{bmatrix} \cos \varphi_0 & \sin \varphi_0 \\ -\sin \varphi_0 & \cos \varphi_0 \end{bmatrix}$ is an in-plane rotation matrix with $\varphi_0 = 0$ for Néel skyrmion here. α is the Gilbert damping and the coefficient $B = \frac{\gamma_0 \hbar \theta_{SHE} L_{sc} I_p}{2eM_s L}$ is linked to the spin Hall effects, being γ_0 the gyromagnetic ratio, \hbar the reduced Planck constant, θ_{SHE} the spin-Hall angle, e the electron charge, M_s the saturation magnetization, L the thickness of the ferromagnetic layer, L_{sc} the scaling length equal to the strip width, and I_p the shape factor of skyrmion.

The solution of Eq. (1) is given (without boundary condition) as,

$$\begin{cases} -gv_y - \alpha D_0 v_x + 4\pi B J_p = 0 \\ gv_x - \alpha D_0 v_y = 0 \end{cases} \quad (2)$$

Then we can obtain the relationship between the velocity of skyrmion and input current pulse

$$v = \sqrt{v_x^2 + v_y^2} = \frac{4\pi B J_p}{\sqrt{\alpha^2 D_0^2 + g^2}}. \quad (3)$$

Therefore, the shift of skyrmion between nearest pinning sites can be described as,

$$S = v \cdot t_p \quad (4)$$

where S is the distance between the nearest pinning sites and t_p is the duration of input current pulse. From Eqs. (3) and (4), one obtains

$$t_p \cdot J_p \cdot \theta_{SHE} = C \quad (5)$$

where $C = SeM_s L \sqrt{\alpha^2 D_0^2 + g^2} / 2\pi \gamma_0 \hbar I_p L_{sc}$ is a constant for a given device. In our system, for $t_p = 1.5$ ns, $J_p = 2 \times 10^{11}$ A/m² and $\theta_{SHE} = 0.4$, $C = 1.2 \times 10^{11}$ ns · A/m² is obtained. The relationship between t_p and J_p is shown in Fig. 4. It is obvious that t_p is inversely proportional to J_p . As mentioned above, large D_E and H_E lead to a relatively strong pinning effect. Although the LEBF potential well can pin the skyrmion, it also

causes a problem when driving the skyrmion. Thus, J_p should be larger than the critical driving current (J_c) to overcome the trapping force and drive the skyrmion out of the LEBF potential well. The influence of D_E and H_E on J_c are similar to that of pinning strength. Therefore, D_E and H_E need to be engineered in order to obtain optimal J_c and J_p [12]. The spin-Hall angle also plays an important role in the device. Antiferromagnets with large spin Hall angle, such as IrMn₃ [35] or PtMn [34], are expected to increase the speed and energy efficiency of the device.

To build a robust device with high performance and energy efficiency, an antiferromagnetic metal with large spin-orbit coupling (providing large enough value of DMI and θ_{SkH_E}) and exchange bias effects under room temperature is necessary. This specific requirement limits the variety of alternative materials. IrMn₃ and PtMn are promising candidates for the antiferromagnetic layer, but other antiferromagnets can also be explored. On the other hand, the initialization of the skyrmions leads to extra energy consumption and operating time, which needs to be optimized. One solution is to increase the spin polarization of the electric current to lower the critical current for writing the skyrmions. The dipolar field originated from the fixed layer of MTJ is neglected in our simulation for simplicity, but for sub-100 nm MTJ the dipolar field may affect the pinning strength and needs to be further modified [12]. By using an optimized MTJ structure, the energy consumption of the initialization operation can be greatly reduced [44]. It is also possible to employ the electric field assisted method to further optimize the device [45].

B. More inputs of instructions

For a programmable logic device, additional inputs of instructions are needed to have more functions. In general, the number of logic functions (N_F) is determined by the number of instructions (N_{INS}). For binary instruction, a device with complete 16 logic functions needs 4 additional inputs of instructions. The 4 terminals in our proposal correspond to the 4 MTJs (in A, B, C, and D sites). For other types of magnetic logic device[13,46-48], it is found that more terminals of instructions lead to more functions, indicating the importance of N_{INS} . Such multi-instructions scheme can also be implemented in the logic devices based on other physical systems, providing a guideline in designing programmable logic device with multiple functions.

V. CONCLUSION

In summary, we proposed a skyrmionic programmable logic device, which includes sixteen types of logic functions. The logic functions are configured by initializing the layout of skyrmions. The pinning sites can enhance the stability and certainty of skyrmion motion, and the device thus shows significant robustness under the effect of inhomogeneity and thermal fluctuations. Our work could stimulate the design of a PLD with complete functions and serve as a candidate for future skyrmionic logic applications.

Acknowledgments

This work is funded by the National Key Research and Development Program of China

(Grant No. 2017YFA0206200), the Science Center of the National Science Foundation of China (No. 52088101), the National Natural Science Foundation of China (NSFC, Grants No.11874409, No. 11804380), the Beijing Natural Science Foundation (Grant No. Z190009), the NSFC-Science Foundation Ireland (SFI) Partnership Programme (Grant No. 51861135104), and the K. C. Wong Education Foundation (No. GJTD-2019-14),. Y.L. also acknowledges support from the Institute of Physics, Chinese Academy of Sciences through the International Young Scientist Fellowship (Grant No. 2018001). R.K.L acknowledges support from Spins and Heat in Nanoscale Electronic Systems (SHINES) an Energy Frontier Research Center funded by the U.S. Department of Energy, Office of Science, Basic Energy Sciences under Award No. DE-SC0012670.

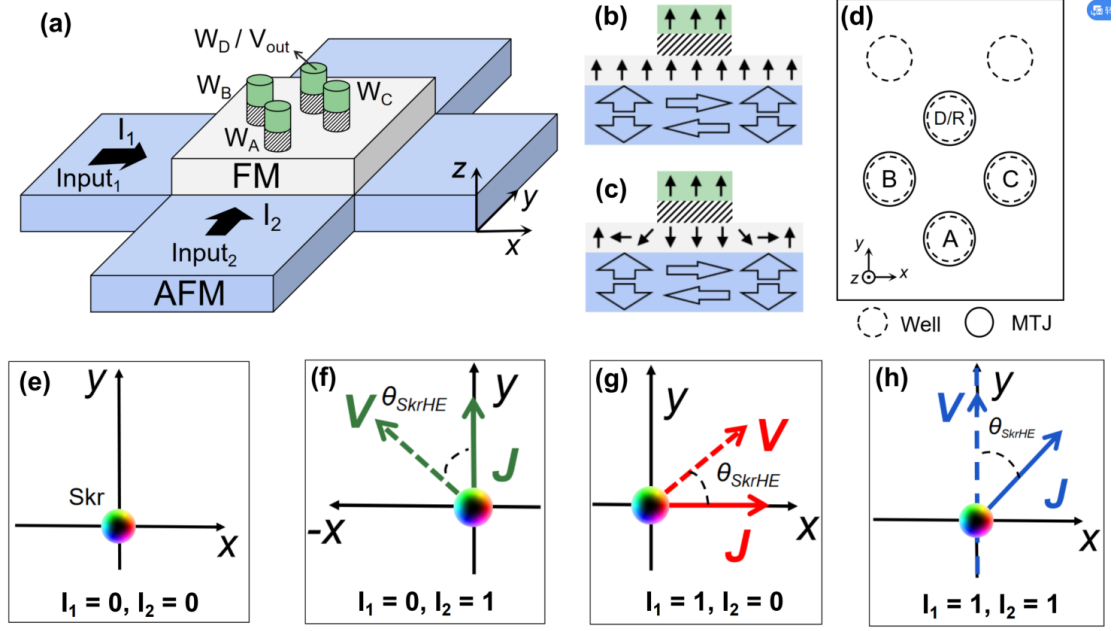


Fig. 1 | Setup of device and motion of skyrmions under input current. **a** Illustration of the device configuration in FM/AFM bilayer. The AFM layer (blue) is patterned into cross-shaped Hall bar and the FM layer (gray) is covered on the center region. Two orthogonal currents with identical amplitude, I_1 and I_2 , are injected into AFM layer as input signals. Four magnetic tunnel junction (MTJ) marked as A, B, C and D are used for writing skyrmions. MTJ D is also used for reading output voltage. **b** and **c** are spin structures in MTJ of parallel (P) and antiparallel (AP) state respectively. Spins in AFM layer are reoriented into local in-plane order resulting in local exchange bias field and pinning sites (PS). **d** Layout of pinning sites and MTJs. **e** - **h** Skyrmion motion in FM layer under different input current. **J** represents the overall current direction and **v** represents the skyrmion velocity. $I_1 = 0$ and $I_2 = 0$ indicate no input current (or equivalently, input 0) leading to no skyrmion motion. $I_1 = 0$ ($I_1 = 1$) and $I_2 = 1$ ($I_2 = 0$) indicate the applied in-plane current flowing along y (x) axis and the skyrmion moves along vector $(-1, 1)$ $[(1, 1)]$. $I_1 = 1$ and $I_2 = 1$ indicate current flow along vector $(1, 1)$

and the skyrmion moves along y axis.

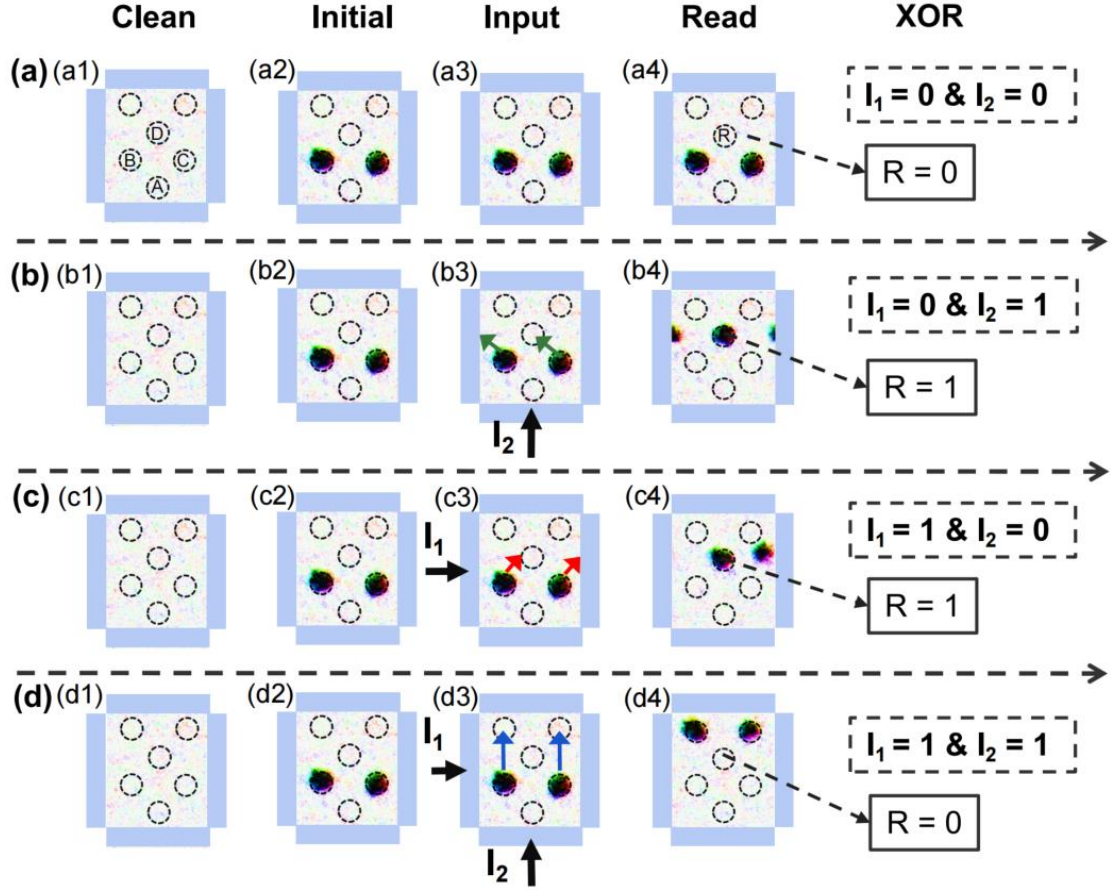


Fig. 2 | Simulated logic device with XOR function. A complete process includes four sets of inputs: **a** $I_1 = 0$ & $I_2 = 0$, **b** $I_1 = 0$ & $I_2 = 1$, **c** $I_1 = 1$ & $I_2 = 0$ and **d** $I_1 = 1$ & $I_2 = 1$, and four operations: clean, initialization (initial for short), input and read. **a1-d1**: ‘Clean’ operation wipes out all skyrmions in FM layers by a large current pulse. **a2-d2**: ‘Initialization’ operation creates skyrmions in specified pinning sites to initialize specific logic function. **a3-d3**: ‘Input’ operation injects the input signals (currents) and drives the skyrmion motion. Black arrows indicate the input currents. The arrows marked by green, red and blue show the trajectory of skyrmions after injecting current. **a4-d4**: ‘Read’ operation reads the output voltage signal from MTJ D. The output signals

‘R’ are indicated by dashed arrows.

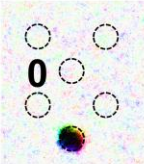
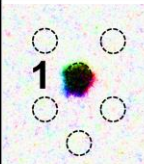
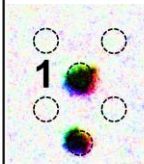
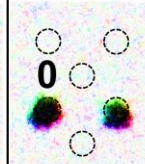
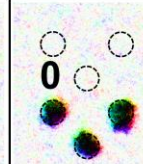
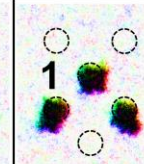
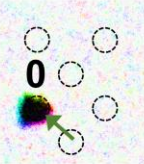
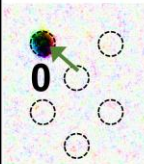
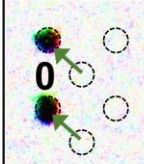
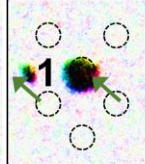
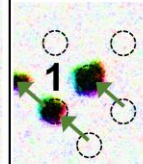
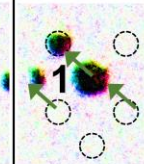
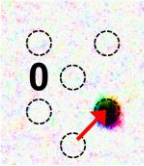
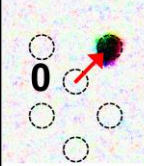
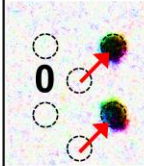
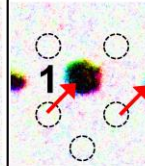
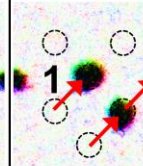
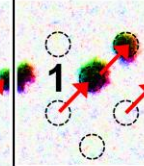
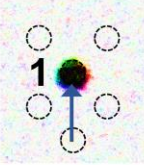
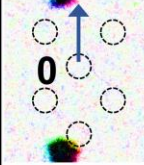
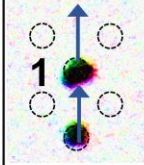
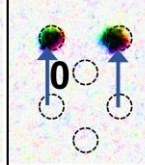
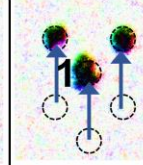
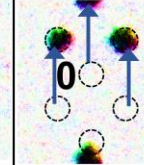
I_1	I_2	A (AND)	D (NOR)	AD (NXOR)	BC (XOR)	ABC (OR)	BCD (NAND)
0	0						
0	1						
1	0						
1	1						

Fig. 3 | Simulated results of different logic functions. The function is configured by setting the skyrmions in specified pinning sites. The corresponding initial states and logic functions (written in the bracket) are shown in the first row. “1” or “0” indicates the output signal from MTJ D. The arrows marked by green, red and blue show the trajectory of skyrmions after injecting different input currents.

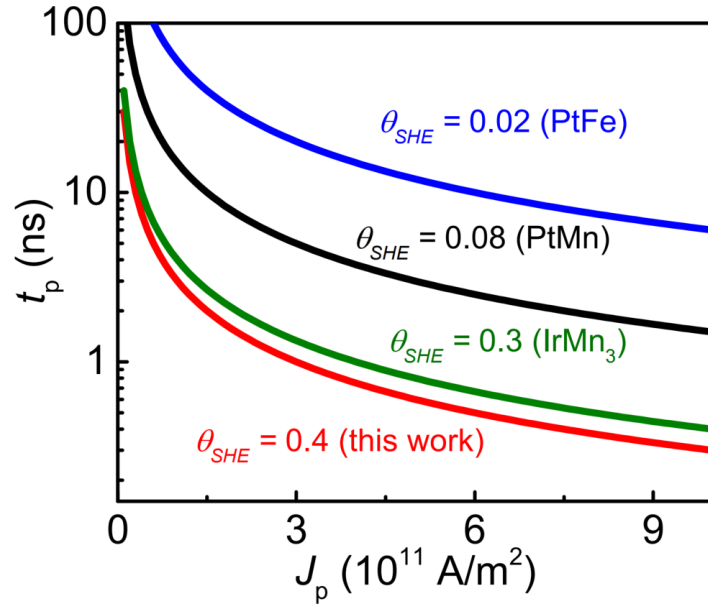
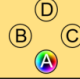


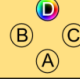










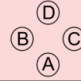



Fig. 4 | Duration of input current (t_p) as a function of the current amplitude (J_p) for various θ_{SHE} . The curves are plotted according to Eq. (6) with different value of θ_{SHE} marked by blue green (0.3 for IrMn₃, Ref. [35]) , black (0.08 for PtMn, Ref. [34])

I_1	I_2	A(AND) 	B(NIMP) 	C(RNIMP) 	D(NOR) 	AB(I_1) 	AC(I_2) 	AD(NXOR) 	BC(XOR) 
0	0	0	0	0	1	0	0	1	0
0	1	0	0	1	0	0	1	0	1
1	0	0	1	0	0	1	0	0	1
1	1	1	0	0	0	1	1	1	0

I_1	I_2	BD(NOT I_2) 	CD(NOT I_1) 	ABC(OR) 	BCD(NAND) 	ACD(IMP) 	ABD(RIMP) 	--(False) 	ABCD(True) 
0	0	1	1	0	1	1	1	0	1
0	1	0	1	1	1	1	0	0	1
1	0	1	0	1	1	0	1	0	1
1	1	0	0	1	0	1	1	0	1

Tab. 1 | Sixteen logic functions programmed by different skyrmion configuration.

Gray cell indicates the input value (I_1 and I_2). The corresponding initial states for different logic function (written in the bracket) are shown in the first row. Orange cells represent the common logic functions. Blue cells indicate material implication. Green cells indicate inoperations and NOT gate. Pink cells represent False and True.

Appendix A: LAYOUT OF PINNING SITES AND MTJS

The skyrmion Hall angle determines the direction of motion of skyrmion under applied current. This machine thus influences the layout of pinning sites and MTJs in the proposed skyrmionic programmable logic device, as shown in Fig. 5 d and h. For $\theta_{SkrHE} \approx 45^\circ$ degree, the layout is shown in Fig. 1 (d) of the main text. For $\theta_{SkrHE} > 45^\circ$ ($\theta_{SkrHE} < 45^\circ$), the layout can be obtained by whole counterclockwise (clockwise) rotation of the one with $\theta_{SkrHE} = 45^\circ$. For example, when the damping constant is 0.01, the skyrmion Hall angle is close to 90 degrees. Thus, the layout of device is rotated about 45 degrees clockwise. The simulation results are shown in Fig. 6. The performance of proposed device is still robust. This also implies that the damping should also be taken into account when optimizing the device.

Appendix B: Micromagnetic simulations with large area and open boundary condition

Fig. 7 shows the simulation results of the XOR gate with sample size $800 \times 800 \times 1$ nm³ and open boundary condition. The results are still robust and similar with that shown in Fig. 2.

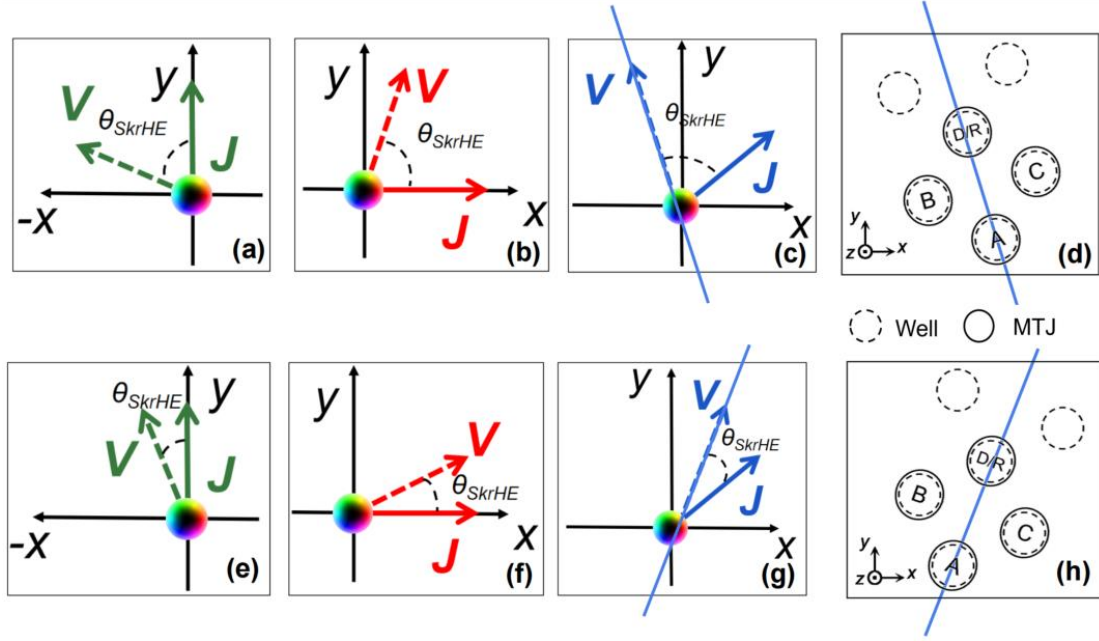


Fig. 5| Sketch of the layout of pinning sites and MTJs in different skyrmion Hall angle. **a-c** and **e-g** are skyrmion motion with small and large skyrmion Hall angle. **d** and **h** are the layouts of pinning sites and MTJs. The solid blue line in **c** and **g** is parallel to **d** and **h**.

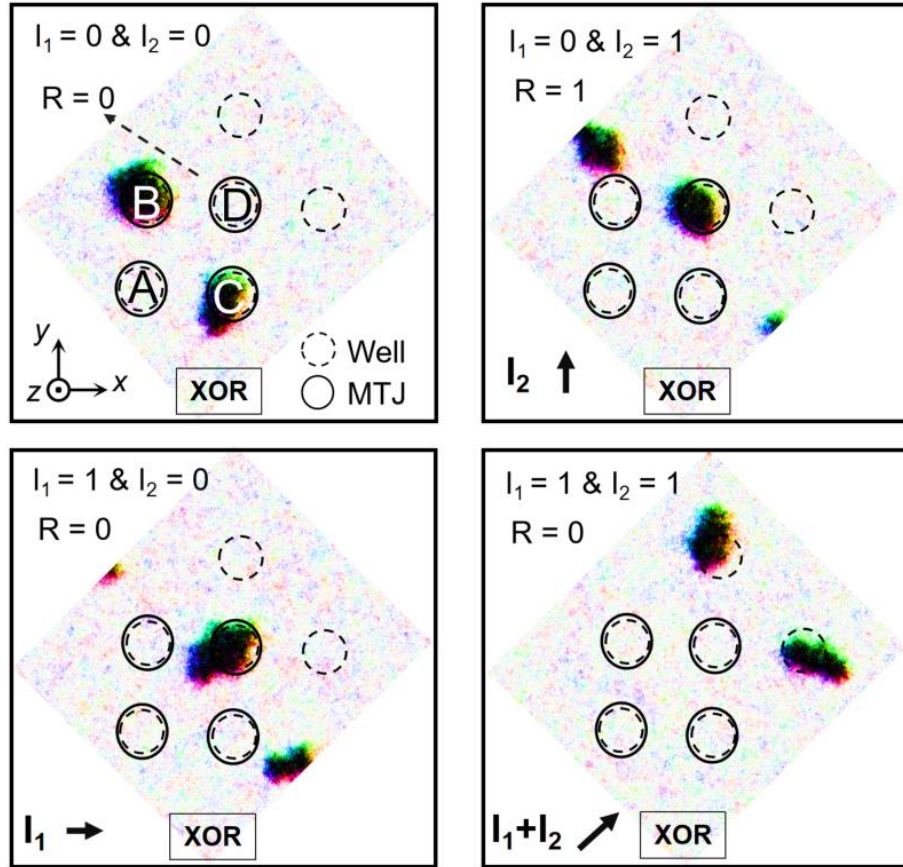


Fig. 6| Simulation results of XOR gate with damping $\alpha = 0.01$.

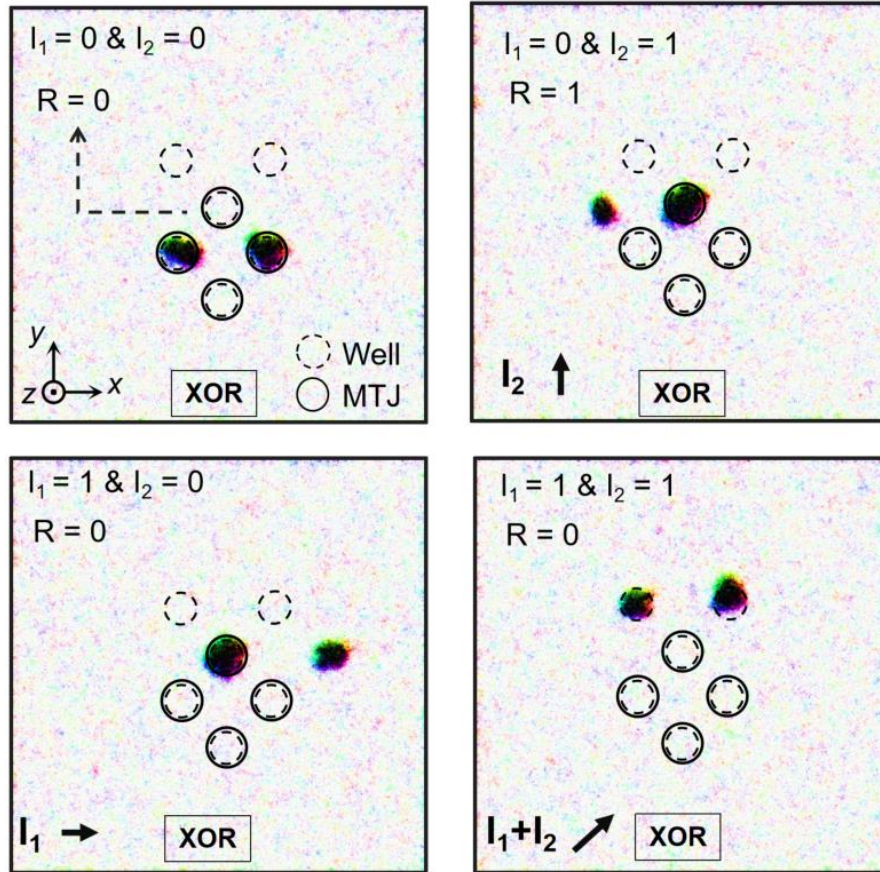


Fig. 7| Simulation results of XOR gate with sample size $800 \times 800 \times 1 \text{ nm}^3$ under open boundary condition.

Reference

- [1] A. Wang and W. D. Woo, Static Magnetic Storage and Delay Line, *J. Appl. Phys.* **21**, 49 (1950).
- [2] M. Kestigian, A. B. Smith, and W. R. Bekebrede, Past, present and future small - bubble - diameter magnetic memory materials, *J. Appl. Phys.* **50**, 2161 (1979).
- [3] G. Y. Chin, New Magnetic Alloys, *Science* **208**, 888 (1980).
- [4] S. S. P. Parkin, M. Hayashi, and L. Thomas, Magnetic Domain-Wall Racetrack Memory, *Science* **320**, 190 (2008).
- [5] A. Fert, V. Cros, and J. Sampaio, Skyrmions on the track, *Nat. Nanotech.* **8**, 152 (2013).
- [6] N. Nagaosa and Y. Tokura, Topological properties and dynamics of magnetic skyrmions, *Nat. Nanotech.* **8**, 899 (2013).
- [7] J. Sampaio, V. Cros, S. Rohart, A. Thiaville, and A. Fert, Nucleation, stability and current-induced motion of isolated magnetic skyrmions in nanostructures, *Nat. Nanotech.* **8**, 839 (2013).
- [8] R. Tomasello, E. Martinez, R. Zivieri, L. Torres, M. Carpentieri, and G. Finocchio, A strategy for the design of skyrmion racetrack memories, *Sci. Rep.* **4**, 6784 (2014).
- [9] R. Wiesendanger, Nanoscale magnetic skyrmions in metallic films and multilayers: a new twist for spintronics, *Nat. Rev. Mater.* **1**, 16044 (2016).
- [10] A. Fert, N. Reyren, and V. Cros, Magnetic skyrmions: advances in physics and potential applications, *Nat. Rev. Mater.* **2**, 17031 (2017).
- [11] G. Yu, P. Upadhyaya, Q. Shao, H. Wu, G. Yin, X. Li, C. He, W. Jiang, X. Han, P. K. Amiri, and K. L. Wang, Room-Temperature Skyrmion Shift Device for Memory Application, *Nano Lett.* **17**, 261 (2017).
- [12] Z. R. Yan, Y. Z. Liu, Y. Guang, J. F. Feng, R. K. Lake, G. Q. Yu, and X. F. Han, Robust Skyrmion Shift Device Through Engineering the Local Exchange-Bias Field, *Phys. Rev. Appl.* **14**, 044008 (2020).
- [13] X. Zhang, M. Ezawa, and Y. Zhou, Magnetic skyrmion logic gates: conversion, duplication and merging of skyrmions, *Sci. Rep.* **5**, 9400 (2015).
- [14] X. Xing, P. W. T. Pong, and Y. Zhou, Skyrmion domain wall collision and domain wall-gated skyrmion logic, *Phys. Rev. B* **94**, 054408 (2016).
- [15] Z. He, S. Angizi, and D. Fan, Current-Induced Dynamics of Multiple Skyrmions With Domain-Wall Pair and Skyrmion-Based Majority Gate Design, *IEEE Magnetics Letters* **8**, 1 (2017).
- [16] S. Luo, M. Song, X. Li, Y. Zhang, J. Hong, X. Yang, X. Zou, N. Xu, and L. You, Reconfigurable Skyrmion Logic Gates, *Nano Lett.* **18**, 1180 (2018).
- [17] H. Yang, C. Wang, X. Wang, X. S. Wang, Y. Cao, and P. Yan, Twisted skyrmions at domain boundaries and the method of image skyrmions, *Phys. Rev. B* **98**, 014433 (2018).
- [18] K. Skahill, *VHDL for Programmable Logic* (Addison-Wesley Longman Publishing Co., Inc., 1996).
- [19] D. A. Allwood, G. Xiong, C. C. Faulkner, D. Atkinson, D. Petit, and R. P. Cowburn, Magnetic Domain-Wall Logic, *Science* **309**, 1688 (2005).
- [20] M. P. Kostylev, A. A. Serga, T. Schneider, B. Leven, and B. Hillebrands, Spin-wave logical gates, *Appl. Phys. Lett.* **87**, 153501 (2005).
- [21] P. Xu, K. Xia, C. Gu, L. Tang, H. Yang, and J. Li, An all-metallic logic gate based on current-driven domain wall motion, *Nat. Nanotech.* **3**, 97 (2008).
- [22] K. A. Omari and T. J. Hayward, Chirality-Based Vortex Domain-Wall Logic Gates, *Phys. Rev. Appl.* **2**, 044001 (2014).
- [23] A. V. Chumak, V. I. Vasyuchka, A. A. Serga, and B. Hillebrands, Magnon spintronics, *Nat. Phys.* **11**, 453 (2015).

- [24] T. Schneider, A. A. Serga, B. Leven, B. Hillebrands, R. L. Stamps, and M. P. Kostylev, Realization of spin-wave logic gates, *Appl. Phys. Lett.* **92**, 022505 (2008).
- [25] T. Liu and G. Vignale, Electric Control of Spin Currents and Spin-Wave Logic, *Phys. Rev. Lett.* **106**, 247203 (2011).
- [26] K. Vogt, F. Y. Fradin, J. E. Pearson, T. Sebastian, S. D. Bader, B. Hillebrands, A. Hoffmann, and H. Schultheiss, Realization of a spin-wave multiplexer, *Nat. Commun.* **5**, 3727 (2014).
- [27] R. Duine, Skyrmions singled out, *Nat. Nanotech.* **8**, 800 (2013).
- [28] J. Iwasaki, M. Mochizuki, and N. Nagaosa, Current-induced skyrmion dynamics in constricted geometries, *Nat. Nanotech.* **8**, 742 (2013).
- [29] X. Zhang, G. P. Zhao, H. Fangohr, J. P. Liu, W. X. Xia, J. Xia, and F. J. Morvan, Skyrmion-skyrmion and skyrmion-edge repulsions in skyrmion-based racetrack memory, *Sci. Rep.* **5**, 7643 (2015).
- [30] W. Jiang, X. Zhang, G. Yu, W. Zhang, X. Wang, M. Benjamin Jungfleisch, John E. Pearson, X. Cheng, O. Heinonen, K. L. Wang, Y. Zhou, A. Hoffmann, and Suzanne G. E. te Velthuis, Direct observation of the skyrmion Hall effect, *Nat. Phys.* **13**, 162 (2016).
- [31] K. Litzius, I. Lemesh, B. Krüger, P. Bassirian, L. Caretta, K. Richter, F. Büttner, K. Sato, O. A. Tretiakov, J. Förster, R. M. Reeve, M. Weigand, I. Bykova, H. Stoll, G. Schütz, G. S. D. Beach, and M. Kläui, Skyrmion Hall effect revealed by direct time-resolved X-ray microscopy, *Nat. Phys.* **13**, 170 (2016).
- [32] J. B. S. Mendes, R. O. Cunha, O. Alves Santos, P. R. T. Ribeiro, F. L. A. Machado, R. L. Rodríguez-Suárez, A. Azevedo, and S. M. Rezende, Large inverse spin Hall effect in the antiferromagnetic metal $\text{Ir}_{20}\text{Mn}_{80}$, *Phys. Rev. B* **89**, 140406 (2014).
- [33] V. Tshitoyan, C. Ciccarelli, A. P. Mihai, M. Ali, A. C. Irvine, T. A. Moore, T. Jungwirth, and A. J. Ferguson, Electrical manipulation of ferromagnetic NiFe by antiferromagnetic IrMn, *Phys. Rev. B* **92**, 214406 (2015).
- [34] Y. Ou, S. Shi, D. C. Ralph, and R. A. Buhrman, Strong spin Hall effect in the antiferromagnet PtMn, *Phys. Rev. B* **93**, 220405 (2016).
- [35] W. Zhang, W. Han, S.-H. Yang, Y. Sun, Y. Zhang, B. Yan, and S. S. P. Parkin, Giant facet-dependent spin-orbit torque and spin Hall conductivity in the triangular antiferromagnet IrMn_3 , *Sci. Adv.* **2**, e1600759 (2016).
- [36] G. Yu, A. Jenkins, X. Ma, S. A. Razavi, C. He, G. Yin, Q. Shao, Q. I. He, H. Wu, W. Li, W. Jiang, X. Han, X. Li, A. C. Bleszynski Jayich, P. K. Amiri, and K. L. Wang, Room-Temperature Skyrmions in an Antiferromagnet-Based Heterostructure, *Nano Lett.* **18**, 980 (2018).
- [37] D. Wu, G. Yu, C.-T. Chen, S. A. Razavi, Q. Shao, X. Li, B. Zhao, K. L. Wong, C. He, Z. Zhang, P. Khalili Amiri, and K. L. Wang, Spin-orbit torques in perpendicularly magnetized $\text{Ir}_{22}\text{Mn}_{78}/\text{Co}_{20}\text{Fe}_{60}\text{B}_{20}/\text{MgO}$ multilayer, *Appl. Phys. Lett.* **109**, 222401 (2016).
- [38] A. A. Thiele, Steady-State Motion of Magnetic Domains, *Phys. Rev. Lett.* **30**, 230 (1973).
- [39] S.-J. Lee, K.-W. Kim, H.-W. Lee, and K.-J. Lee, Spin-orbit-torque-induced skyrmion dynamics for different types of spin-orbit coupling, *J. Magn. Magn. Mater.* **455**, 14 (2018).
- [40] E. Albisetti, D. Petti, M. Pancaldi, M. Madami, S. Tacchi, J. Curtis, W. P. King, A. Papp, G. Csaba, W. Porod, P. Vavassori, E. Riedo, and R. Bertacco, Nanopatterning reconfigurable magnetic landscapes via thermally assisted scanning probe lithography, *Nat. Nanotech.* **11**, 545 (2016).
- [41] Y. Guang, I. Bykova, Y. Liu, G. Yu, E. Goering, M. Weigand, J. Gräfe, S. K. Kim, J. Zhang, H. Zhang, Z. Yan, C. Wan, J. Feng, X. Wang, C. Guo, H. Wei, Y. Peng, Y. Tserkovnyak, X. Han, and G. Schütz, Creating zero-field skyrmions in exchange-biased multilayers through X-ray illumination, *Nat.*

Commun. **11**, 949 (2020).

- [42] Y. Guang, Y. Peng, Z. Yan, Y. Liu, J. Zhang, X. Zeng, S. Zhang, S. Zhang, D. M. Burn, and N. Jaouen, Electron beam lithography of magnetic skyrmions, *Adv. Mater.* **32**, 2003003 (2020).
- [43] A. Vansteenkiste, J. Leliaert, M. Dvornik, M. Helsen, F. Garcia-Sanchez, and B. Van Waeyenberge, The design and verification of MuMax3, *AIP Advances* **4**, 107133 (2014).
- [44] X. Chen, H. Zhang, E. Deng, M. Yang, N. Lei, Y. Zhang, W. Kang, and W. Zhao, Sky-RAM: Skyrmionic Random Access Memory, *IEEE Electron Device Letters* **40**, 722 (2019).
- [45] J.-M. Hu, Z. Li, L.-Q. Chen, and C.-W. Nan, High-density magnetoresistive random access memory operating at ultralow voltage at room temperature, *Nat. Commun.* **2**, 553 (2011).
- [46] Z. Luo, A. Hrabec, T. P. Dao, G. Sala, S. Finizio, J. Feng, S. Mayr, J. Raabe, P. Gambardella, and L. J. Heyderman, Current-driven magnetic domain-wall logic, *Nature* **579**, 214 (2020).
- [47] X. Zhang, C. H. Wan, Z. H. Yuan, C. Fang, W. J. Kong, H. Wu, Q. T. Zhang, B. S. Tao, and X. F. Han, Experimental demonstration of programmable multi-functional spin logic cell based on spin Hall effect, *J. Magn. Magn. Mater.* **428**, 401 (2017).
- [48] W. Yu, J. Lan, and J. Xiao, Magnetic Logic Gate Based on Polarized Spin Waves, *Phys. Rev. Appl.* **13**, 024055 (2020).